ACS NANO

www.acsnano.org

Understanding and Controlling Structural Defects and Disordering in $LiNi_{0.5}Mn_{1.5}O_4$ Cathodes for Direct Recycling

Hongpeng Gao, Bing Han, Duc Tran, Luqi Zhang, Zishuo Zhao, Yu-ting Chen, Wei Tang, Mingjie Xu, Junlin Wu, Xiaolu Yu, Varun Gupta, Maura Appleberry, Haodong Liu, Yijie Yin, Weiliang Yao, Mingqian Li, Weikang Li, Linqin Mu, Ying Shirley Meng, and Zheng Chen*

Cite This: *ACS Nano* 2024, 18, 30737−30748

Read Online

ACCESS | Metrics & More | Article Recommendations | Supporting Information

ABSTRACT: **Despite significant progress in recycling spent lithium-ion batteries (LIBs), nondestructive, direct recycling methods still face untenable discrepancies in multiple cathode chemistries, which primarily originate from a variety of structure stabilities during the recycling process. Through systematic investigation of the microstructure evolution during the relithiation treatment, we observed the inevitably induced defects and Li/Mn disordering in the $LiNi_{0.5}Mn_{1.5}O_4$ cathode, contributing to the sluggish Li^+ transport and irreversible capacity loss. Employing a defect engineering approach to achieve twin boundaries and preferred grain orientation, we show the regenerated cathodes demonstrate a substantial enhancement of Li^+ diffusion and cycling stability, retaining 97.4% capacity after 100 cycles and 87.96% after 200 cycles at C/3. This work not only elaborates on a systematic investigation of defect inducement and structural restoration mechanism but also provides an effective approach to directly recycle high-voltage spinel-type cathodes, contributing to the sustainability of next-generation LIBs.**

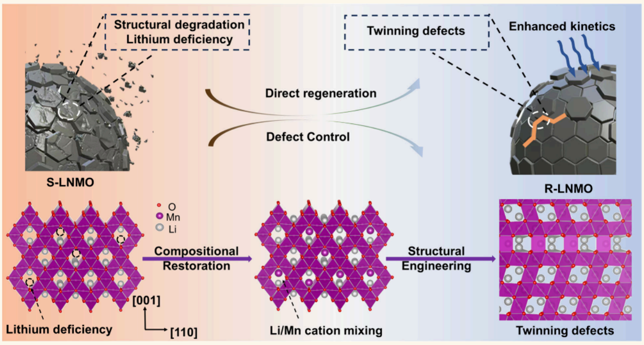

KEYWORDS: *direct recycling, spinel structure, Li/Mn disordering, defect engineering, twin boundary*

The widespread adoption of electric vehicles (EVs) using lithium-ion batteries (LIBs) is a vital step in moving toward a sustainable energy and carbon neutrality future.[1] There is a growing demand for high power and energy densities in LIBs to increase the driving range of EVs.[2] As the most valuable part, the cathode material constitutes more than 40% of both cost and weight ratios when considering all components in LIBs.[3] Current efforts in both research and commercialization related to cathode materials primarily center on three categories: lithium metal oxides with a layered structure, such as lithium nickel cobalt manganese oxide ($LiNi_xCo_yMn_zO_2$, where $x + y + z = 1$, referred to as NCM), lithium iron phosphate ($LiFePO_4$, known as LFP) with an olivine structure, and lithium manganese oxides ($LiMn_2O_4$, LMO) with a spinel structure.[4] Layered lithium metal oxides offer high energy densities, but their widespread use causes concern with expensive and environmentally harmful cobalt elements, especially when considering the broader adoption of electric vehicles.[5] Cobalt-free cathodes, such as LFP and LMO, provide relatively lower energy density (<500 Wh/kg at the material level), which might fall short of the requirements for long-range electric vehicles.[6] Cobalt-free, lithium- and manganese-rich layered oxide materials have also garnered significant attention due to their impressive energy density, but there remain challenges related to their limited phase reversibility during cycling, primarily due to issues originating from stoichiometric oxygen loss.[7]

$LiNi_{0.5}Mn_{1.5}O_4$ (LNMO), a derivative of LMO through nickel substitution, presents an appealing substitute. Ni substitution enhances the operating voltage of the parent LMO cathode from 4 V to ~4.8 V (vs Li/Li^+) consequently increasing the theoretical energy density from 480 to 620 Wh/kg, leveling with the NCM cathodes.[8] Nonetheless, the LNMO

Received: July 27, 2024
Revised: October 6, 2024
Accepted: October 9, 2024
Published: October 21, 2024

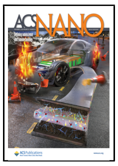

https://doi.org/10.1021/acsnano.4c10164
ACS Nano 2024, 18, 30737−30748

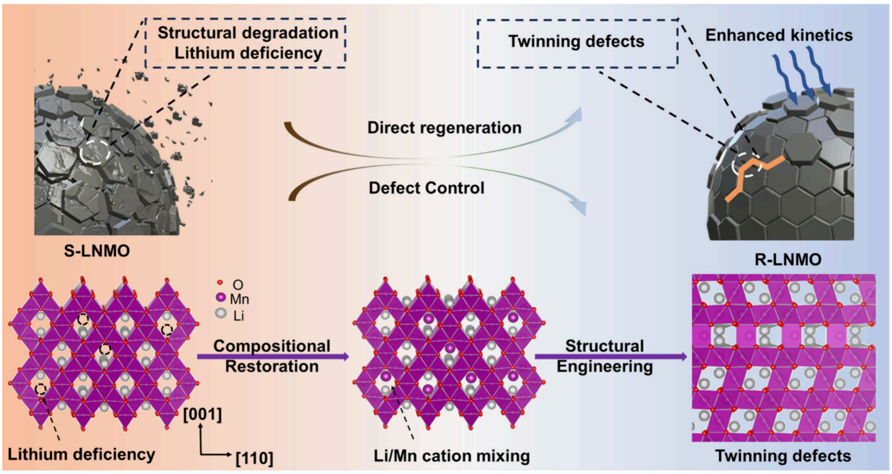

Figure 1. Schematic illustration of the direct regeneration of LNMO cathodes with defect control. A hydrothermal treatment in LiOH solution is applied to spent LNMO particles to compensate for the lithium loss in spent LNMO powders. Following an optimal short annealing step, the regenerated LNMO particles are obtained with induced defects, e.g., twin boundaries and preferred lattice orientation, resulting in distinctive Li^+ diffusion kinetics.

still encounters some obstacles, such as inferior electronic conductivity,[9] fast capacity degradation,[10] and issues with the current carbonate electrolyte system stemming from its high operating voltage.[11] Though there is a deep history in the literature on efforts to mitigate the Jahn−Teller distortion and disproportion reaction of Mn^{3+}, avoiding such complex cross-talking phenomena remains an immense challenge.[12,13] One effective approach is the control of Mn^{3+} content to safeguard the surface against deteriorating acidic reactions from liquid electrolytes.[14] Thus far, researchers have primarily concentrated on modifying the surface through techniques such as elemental doping, interfacial adjustments,[15] and electrolyte engineering[16] to improve the aforementioned drawbacks thereby improving the cycling stability and rate performance. On the other hand, by understanding LNMO degradation mechanisms, defect engineering can be applied to regulate Mn^{3+} content and enhance the electrochemical performance.[17]

Despite decades of research that has unveiled the degradation mechanism of LNMO cathodes, there has been limited investigation into the healing or repairing of these cathodes. As a cobalt-free, low-cost cathode material, conventional hydrometallurgical and pyrometallurgical recycling processes—which are energy-intensive, costly, and generate significant waste—are not viable for economically recycling LNMO.[18] The emerging direct recycling technology, starting with a relithiation step to produce rejuvenated cathode active materials, has gained increasing attention due to its minimal energy consumption and maximum profitability when recycling materials like NCM,[19,20] LFP,[21] LMO,[22] and $LiNi_{0.88}Co_{0.095}Al_{0.025}O_2$ (NCA).[23] Among various relithiation methods (such as solid-sintering,[24] molten salt,[25] ionothermal,[26] and redox mediation[27]), hydrothermal treatment[20] stands out as the most versatile process, demonstrating self-saturation in various structures (spinel,[22] olivine,[28] and layered structure[29]). With its high effectiveness, low cost, and potential scalability, hydrothermal relithiation treatment is a suitable approach for investigating the rejuvenation mechanism of LNMO.

Understanding the structural evolution of spinel-type cathodes through the direct recycling process is crucial for advancing next-generation battery recycling. As cathode materials undergo resynthesis and experience regrowth of grains during the recycling process, the introduction of cation disordering, antisites, and dislocations gives rise to distinctive electrochemical properties. Previous studies have demonstrated that the elaboration of defects can bring about a transformative effect on the performance of spinel-type cathodes.[30] Consequently, identification of a systematic structural repair mechanism for such cathodes becomes imperative for comprehending the electrochemical properties related to its structure and fully revitalizing its performance. Despite the existence of various strategies for recycling optimization, many phenomena associated with cathode direct recycling still await complete discovery and resolution.

Herein, we provide a thorough analysis of the healing mechanism of spent LNMO cathodes encompassing relithiation and structure reconstruction. We present clear evidence of Li/Mn disordering layers induced during an aqueous relithiation process, resulting in significant capacity loss and insufficient reversible capacity. To address these issues, we systematically rectify these failures through careful design of post-annealing conditions. By introducing abundant twin boundaries and preferred grain orientation in spinel lattice structures, we successfully rejuvenate the electrochemical activity of degraded LNMO cathodes. Notably, the resulting regenerated LNMO demonstrates a significant enhancement in its rate performance without sacrificing energy density, retaining 97.4% capacity after 100 cycles at C/3, comparable to the pristine LNMO. This effective direct recycling method, employing defect engineering, not only reveals the healing mechanism in spinel structures but also provides insights for designing synthetic strategies of next-generation sustainable LIBs.

RESULTS AND DISCUSSION

Compositional and Structural Restoration of the Spent LNMO Cathodes. Defect engineering has shown effectiveness in tuning the electrochemical performance of spinel cathodes by regulating the oxygen deficiency,[31−33] transition metal ordering,[34,35] and crystallographic properties.[36,37] Additionally, the mechanism of compositional repair in spent LMO cathodes has been well elucidated in our

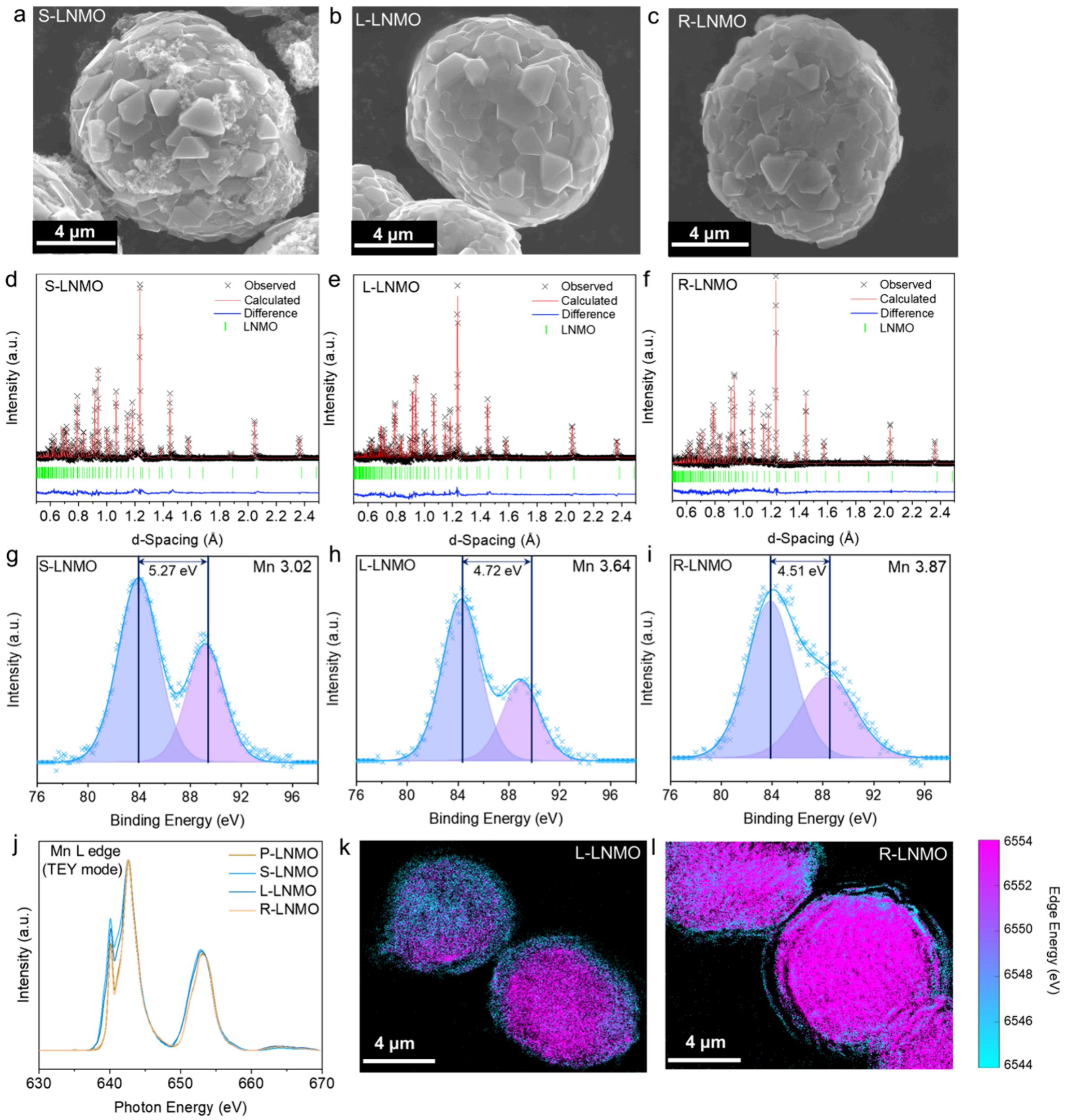

Figure 2. The phase identification and structural dynamics during the regeneration process. SEM images of (a) S-LNMO, (b) L-LNMO, and (c) R-LNMO. The Rietveld refinement neutron diffraction patterns of (d) S-LNMO, (e) L-LNMO, and (f) R-LNMO. The Mn 3s XPS spectra of (g) S-LNMO, (h) L-LNMO, and (i) R-LNMO. (j) Mn L-edge soft XAS spectra of the LNMO particles of interest. The 2D XANES mapping images of Mn in (k) L-LNMO and (l) R-LNMO.

previous work.[22] In this work, we successfully rejuvenated spent LNMO cathodes with abundant defects by a hydrothermal treatment and optimized annealing conditions. The structural evolution of the LNMO cathodes is illustrated in Figure 1. Briefly, the spent LNMO cathodes (named as "S-LNMO") are harvested from a multilayer LNMO/graphite pouch cell (>3 Ah) by the method reported in our previous work.[38] The obtained spent cathode particles with both compositional and structure degradation are subjected to hydrothermal treatment (denoted as "L-LNMO") under different conditions for relithiation purposes. Following a short annealing process at the optimized temperature, regenerated LNMO particles (denoted as "R-LNMO") are obtained, featuring the presence of twinning defects with substantial enhancement of Li^+ diffusion.

The lithiation mechanism for restoring the composition of the spent LNMO was elucidated by inductively coupled plasma quadrupole mass spectrometry (ICP-MS) measurements of S-LNMO and samples subjected to lithiation treatment with varying concentrations of LiOH (Figure S1). Note that a 30% lithium deficiency was observed after 300 cycles in a voltage range of 2.8−4.8 V at 0.33C in the multilayer LNMO/graphite pouch cells (Figure S2). An ideal composition ($Li_{1.020}Ni_{0.460}Mn_{1.540}O_4$) can be achieved, which is comparable to the pristine level ($Li_{1.001}Ni_{0.453}Mn_{1.524}O_4$) by optimized relithiation kinetic control in hydrothermal treatment with 1 M LiOH solution (Table S1). After the short-term annealing step at the designed temperature, the R-LNMO has no significant variation in terms of composition compared with that in L-LNMO.

https://doi.org/10.1021/acsnano.4c10164
ACS Nano 2024, 18, 30737−30748

Scanning electron microscopy (SEM) images have been examined to demonstrate the efficacy of our regeneration method. Figure 2a−c and Figure S3 display the S-LNMO, L-LNMO, R-LNMO, and P-LNMO under optimized conditions. These images reveal that the S-LNMO particles did experience some cracking issues during extended cycling. Following an effective regeneration process, the morphology of R-LNMO was successfully restored to its pristine level. This suggests a resolution of the cracking problem by crystal regrowth during the annealing process. From the neutron diffraction patterns (Figure 2d−f and Figure S4), the peak positions in all samples are well matched with the standard pattern of a $Fd\bar{3}m$ space group.[39] Additionally, Rietveld refinement was carried out on all neutron diffraction patterns using the GSAS software with EXPGUI as the graphical user interface (Table S2). The unit cell lattice parameter in S-LNMO decreases from 8.179 to 8.147 Å (compared to P-LNMO), due to a 30% loss of lithium. This shrinkage indicates a low packing fraction caused by the reduced number of atoms and the sizes difference of cations (Ni^{2+} = 69 pm, Ni^{3+} = 53 pm, and Ni^{4+} = 48 pm).[40,41] After the lithiation process, an enlarged lattice parameter was observed, despite the sample having a similar stoichiometry to the pristine material, suggesting the presence of Li/transition metal (Li/TM) disordering, which contributes to the loose packing of the unit cell. The hydrothermally treated sample exhibits significant Li/TM mixing in 8a sites (2.89%) compared with P-LNMO (0.56%). In contrast, R-LNMO achieves lattice parameter shrinkage through a short annealing step. This process facilitates cation diffusion and heals oxygen deficiencies, especially at high temperatures in a pure oxygen atmosphere.[34,42]

X-ray photoelectron spectroscopy (XPS) was conducted on the treated LNMO particles to verify the valence changes in the transition metals. The Mn 3s spectra, as depicted in Figure 2g−i, were fitted to illustrate the evolution of the average oxidation state (AOS) of Mn. This analysis involved assessing the difference in binding energy between peaks (ΔE) and using the equation[43] AOS = 8.956−1.126 ΔE to approximate the average Mn oxidation state. As shown in Figure S5, a significant amount of Ni^{3+} exists in S-LNMO. Despite a ∼30% lithium loss in spent materials, the Mn valence in S-LNMO drops from +3.76 to +3.02 due to the high AOS of Ni. The elevated Mn valence is observed following relithiation treatment in LiOH solutions of varying concentrations. The AOS of Mn increased from +3.02 to +3.10, + 3.64, and +3.41 after relithiation in 0.1, 1, and 4 M LiOH solutions (referred to as "L-LNMO-1", "L-LNMO-2", and "L-LNMO-3", respectively) (Figure S6). Although Ni^{3+} remains dominant on the L-LNMO surface after relithiation (Figure S5), the increase in the Mn valence is attributed to repaired oxygen vacancies in the LNMO particles. Figure S7 illustrates a notable growth of a side peak at ∼531 eV, reflecting the mitigation of oxygen defects after relithiation treatment.[31] Additionally, these oxygen vacancies are reduced to pristine levels following the annealing step under an oxygen flow. As indicated by a reduction of Mn valence in L-LNMO-3, the spinel structure became unstable, entering an overlithiated status during hydrothermal treatment with LiOH concentrations exceeding 1 M. The impurity phase can be identified as Li_2MnO_3 based on the XRD pattern of the L-LNMO-3 (Figure S8), This phenomenon has also been reported in $LiMn_2O_4$ regeneration by the hydrothermal reaction.[22] However, following a short annealing step, Mn and Ni valences were successfully restored to the pristine level in R-LNMO. This outcome is corroborated by Raman spectra in Figure S9, in which two characteristic Ni−O stretching bands at 390 and 491 cm^{-1} are detected, representing the E_g and $F_{2g}{}^2$ vibrational modes in the spinel structure. Additionally, a Mn−O symmetric stretching vibration is observed at 630 cm^{-1}, confirming the A_{1g} vibration in the MnO_6 octahedra.[44] A small peak at 546 cm^{-1} related to the $F_{2g}{}^1$ vibrational mode is observed as well, indicating that the as-prepared LNMO samples can be indexed to the $Fd\bar{3}m$ space group (disordered spinel with high symmetry).[13] Notably, the overlithiated sample (L-LNMO-3) displays an indistinct $F_{2g}{}^1$ peak, suggesting a compromised symmetry in the spinel structure. Furthermore, the L-LNMO samples exhibit a broad A_{1g} peak, indicative of multiple vibration modes in MnO_6 octahedra due to the mixture of Mn valence status. In contrast, the R-LNMO demonstrates a significant improvement in the sharpness of the A_{1g} peak. This enhancement underscores the crucial role played by the annealing step in reconstructing the well-defined lattice structure, signifying its importance in reversing the adverse effects caused by the overlithiated status during hydrothermal treatment.

Via soft X-ray absorption spectroscopy (XAS), we compared the surface Mn states of the LNMO particles, delving deeper into the valence distribution of transition metals during the regeneration process. All the LNMO particles exhibit a characteristic of Mn(IV), shown in Figure. 2j. The presence of side peak around 640 eV indicates the lower valence of Mn at the surface in S-LNMO and L-LNMO.[45] The fluorescence-yield (FY) mode had a probing depth of 50 nm. Comparison of the TEY and FY mode demonstrates the abundance of Mn(III) in L-LNMO, which could be eliminated by following the regeneration process (Figure S10). Furthermore, 2D X-ray absorption near-edge structure (XANES) mapping with a resolution of 28.7 nm per pixel was conducted to provide a detailed investigation into the edge energy distribution of Mn, revealing elemental restoration. As depicted in Figure 2k, the 2D XANES mapping shows a lower near-edge energy of Mn near the surface of the L-LNMO particles, confirming previous findings obtained through surface-sensitive technologies such as XPS and Raman spectroscopy. Following the annealing step, the near-edge energy of Mn shifts to a higher energy level with good uniformity (Figure 2l). Despite the stoichiometric composition obtained through this effective recycling method, a more detailed examination of structure evolution in LNMO particles is necessary to fully understand the influence of defect controlling on performance.

Identification and Mitigation of Li/Mn Disordering. To comprehend the remaining issue of samples obtained from hydrothermal treatment (without annealing) with stoichiometric composition, a detailed structural analysis was undertaken through neutron diffraction. As mentioned earlier, this analysis provides insights into atomic occupancy, with Li^+ typically occupying tetrahedral 8a sites and Mn/Ni ions occupying octahedral 16d sites in a typical face-centered cubic $Fd\bar{3}m$ structure. Moreover, the refinement results reveal significant site occupancies of Mn ions at the 8a sites in L-LNMO particles, causing significant Li/Mn cation mixing (2.89%). In contrast, only 0.56% and 0.47% Li/Mn mixing are observed in P-LNMO and R-LNMO samples (Table S2). This substantial Li/Mn cation disorder aligns with the result of the structural failure discussed earlier.

The atomic arrangement of L-LNMO particles was examined by using high-angle annular dark field scanning

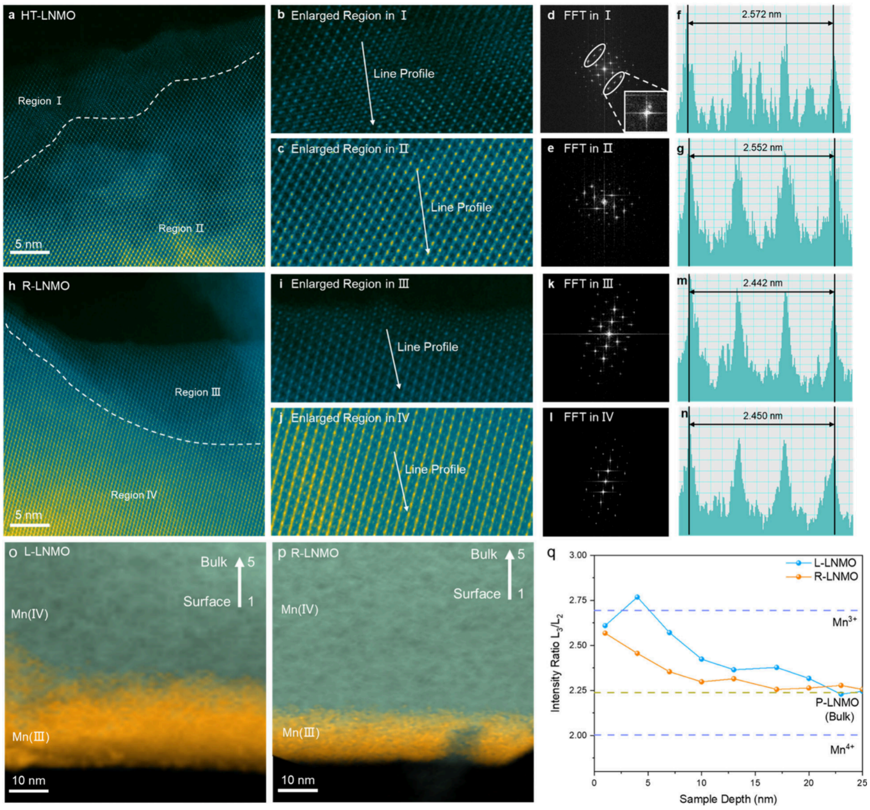

Figure 3. The observation of Li/Mn disordering and microstructure change in treated LNMO particles. (a) HRTEM image, (b, c) enlarged figures, (d, e) fast Fourier transform (FFT) images, and (f, g) line profiles in b and c of L-LNMO. (h) HRTEM image, (i, j) enlarged figures, (k, l) fast Fourier transform (FFT) images and (m, n) line profiles in i and j of R-LNMO. (o, p) The HAADF-STEM-EELS mapping images and (q) spatially resolved intensity ratio of the L_3/L_2 peak from surface to bulk of L-LNMO and R-LNMO.

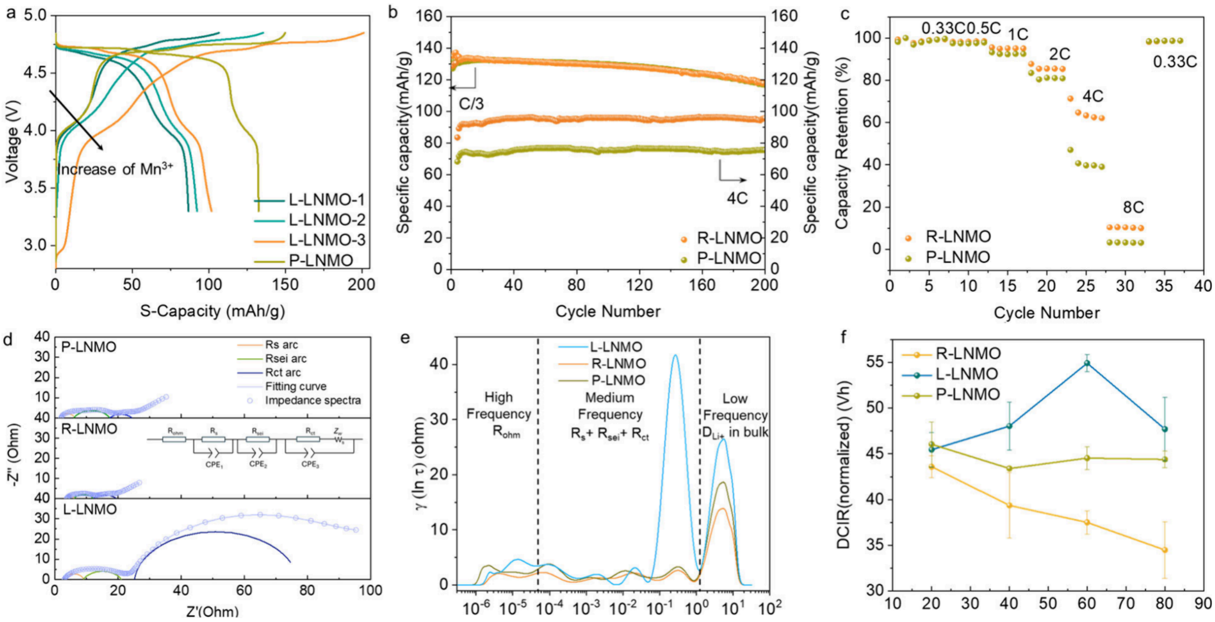

Figure 4. The electrochemical properties evaluation of different LNMO samples. (a) Voltage profile of P-LNMO and L-LNMO particles in different relithiation conditions. (b) Cycling performance of S-LNMO, P-LNMO, and R-LNMO at C/3 and 4C. (c) Rate performance of P-LNMO and R-LNMO. (d) EIS fitting and (e) DRT analysis of P-LNMO, L-LNMO, and R-LNMO at 100% SOC. (f) DCIR result of P-LNMO, L-LNMO, and R-LNMO at different SOCs.

transmission electron microscopy (HAADF-STEM) to investigate the presence of Li/Mn disordering on the surface. As STEM images reflect the Z-contrast of materials, Figure 3a demonstrates a well-defined spinel structure in the bulk area (Region II), with the positions of transition metals (16d sites) resolved atomically along the [110] zone axis. In Figure 3b–c, a significant reorganization of the atomic arrangement and lattice structure distortion is evident in the surface region (Region I). Additionally, the fast Fourier transform (FFT) image in Figure 3d−e displays duplicated bright dots with an ellipse shape (marked by a white circle), indicating lattice distortion and phase impurity in the surface area of L-LNMO. Note that lithium (8a sites) and oxygen (32e sites) are not visible in the Z-contrast STEM image due to their low atomic masses. Upon close observation of the images, the corresponding line profiles illustrate the atomic arrangement intuitively in four selected unit cells near the surface. Figure 3f reveals a notable intensity at the Li position, indicating the occupancy of the transition metal ion in 8a sites near the surface of L-LNMO, while a well-defined spinel-type lattice is shown in the bulk area (Figure 3g). To eliminate the Li/Mn disordering, an annealing treatment is applied to reconstruct the lattice structure. As shown in Figure 3h, a uniform feature is revealed in R-LNMO particles from bulk to the surface. No lattice distortion or cation disorder exists in the enlarged images (Figure 3i−j). Moreover, the FFT images (Figure 3k−l) and line profiles (Figure 3m−n) illustrate the effectiveness of reconstruction via the annealing step.

A combination of HAADF-STEM and Electron Energy Loss Spectroscopy (EELS) was employed to gain further insights into Li/Mn structural defects. The HAADF-STEM images provide spatial information correlated to the recorded spectrum. As a fingerprint for the oxidation state of Mn, an EELS mapping combined with L_3/L_2 peak ratio analysis is applied to P-LNMO, L-LNMO, and R-LNMO, using pure Mn_2O_3 and MnO_2 as references. The resulting mapping, as shown in Figure 3o, reveals a thicker low-valence layer of Mn near the surface in L-LNMO. In contrast, Figure 3p illustrates that the Mn valence mapping of R-LNMO shows a similar thickness compared with the P-LNMO materials (Figure S11), indicating the attainment of a stable structure with the desired valence of Mn. The L_3/L_2 peak ratio of Mn extracted in the EELS spectra, spanning from the surface to the bulk, is illustrated in Figure 3q. Notably, the increase in the peak ratio of Mn L_3/L_2 from bulk to surface suggests a reduction of bulk Mn^{4+} to Mn^{3+} on the surface of L-LMNO particles.[46] On the other hand, R-LNMO illustrates a thinner Mn transition zone and a similar ratio as the bulk signal of P-LNMO. Therefore, a short annealing step has successfully reconstructed the well-defined spinel lattice, reversing the adverse effects caused by Li/Mn disordering during lithiation treatment.

Electrochemical Response of Treated LNMO Particles. The electrochemical performance of different LNMO cathodes was further assessed through half cells within the potential range of 3.0 to 4.85 V (vs Li/Li^+). The performance of S-LNMO as collected was found to have a discharge capacity of less than 60% compared to that of P-LNMO (Figure S12). As depicted in Figure 4a, the treated LNMO contains a portion of Mn^{3+}, which is oxidized to the Mn^{4+} state at the beginning of charging, resulting in a voltage plateau at around 4.1 V (vs Li/Li^+). With an increased LiOH concentration during hydrothermal treatment, the plateau around 4.1 V contributes to more charge capacity in the initial formation cycle. However, this irreversible capacity, stemming from excess Mn^{3+} oxidation generated by overlithiation during hydrothermal treatment, is entirely lost in the subsequent discharge cycle. Thus, despite having a sufficient amount of lithium in the lattice, the electrochemical performance cannot be fully recovered through only hydrothermal treatment.

We implemented a systematic investigation on the annealing process to optimize the electrochemical performance of R-LNMO. To avoid the oxygen deficiency during the regeneration, an oxygen atmosphere was chosen to heal the defects of the remaining low-valence Mn^{3+} after hydrothermal treatment. Varying degrees of cation ordering in R-LNMO cathodes are obtained in different temperatures after 4 h annealing under 650, 750, 850, and 950 °C (referred as "R-LNMO-1", "R-LNMO-2", "R-LNMO-3", and "R-LNMO-4"). As depicted in Figure S13, the Mn^{3+} plateau tends to diminish after annealing in an oxygen atmosphere at all temperatures. R-LNMO-1 and R-LNMO-2 exhibit a higher degree of cation ordering than R-LNMO-3, likely due to the proximity to the phase transition temperature of ordered/disordered LNMO. A more detailed analysis using dQ/dV versus V plots reveals two peaks around 4.7 V (Figure S14), indicating the two-step oxidation or reduction for the Ni^{2+}/Ni^{4+} redox couple. The separation between these peaks reflects the disordered/ordered phases, with a narrower separation indicating a higher degree of cation ordering.[47] In Figure S15, a worse cycling stability is observed in R-LNMO-2 and R-LNMO-1, attributed to their high degree of cation ordering, which leads to poor electronic conductivity in ordered LNMO cathodes.[48] The proportion of ordered and disordered phases in the sintered samples was further analyzed qualitatively by using Raman spectroscopy (Figure S16). Among the sintered LNMO samples, R-LNMO-2, sintered at 750 °C, exhibited the most distinct Eg vibrational mode around 400 cm^{-1}, indicating the most ordered structure. This resulted in the worst cycling stability and the narrowest dQ-dV peak splitting. With an optimized temperature, R-LNMO demonstrated a cycling performance similar to the pristine sample, retaining 97.4% capacity after 100 cycles and 87.96% after 200 cycles at a C/3 rate (Figure 4b). Additionally, Figure 4c highlights the superior rate performance of R-LNMO compared to that of the pristine sample. Notably, R-LNMO maintained stable cyclability at a 4C rate, delivering 92.6 mAh/g, in contrast to 73.7 mAh/g in the pristine sample. However, as shown in Figure S17, the enhanced rate performance was diminished when higher annealing temperatures were applied in R-LNMO-4. Therefore, this distinctive electrochemical performance is attained by effectively adjusting the Mn^{3+} content through an optimized annealing process.

A comprehensive electrochemical analysis was carried out to further understand the divergence in kinetic dynamics. We conducted an electrochemical impedance spectroscopy (EIS) analysis with the distributions of relaxation times (DRT) calculation and direct current internal resistance (DCIR) to unveil the improvement in Li^+ kinetics in regenerated LNMO cathodes. EIS measurements were performed under different states of charge (SOC) during the charging process, as shown in Figure S18. The observed three semicircles correspond to the resistance of the contact interface (R_s), solid-electrolyte interface (R_{sei}), and charge transfer (R_{ct}) from high to low frequency. Consistent with the enhanced high-rate performance, a smaller R_{ct} value (7.41 Ohm) was observed in R-LNMO compared to it (12.86 Ohm) in P-LNMO (Table S3). On the other hand, the enlarged R_{ct} value (51.59 Ohm) in L-LNMO (Figure 4d and 4e) indicates that the hydrothermally treated sample exhibits significantly increased resistance, due to the abundance of mentioned lattice defects. Nevertheless, at both 60% SOC and 100% SOC, R-LNMO demonstrates the lowest resistance compared to P-LNMO, indicating faster kinetics in the bulk and interface (Figure S19).

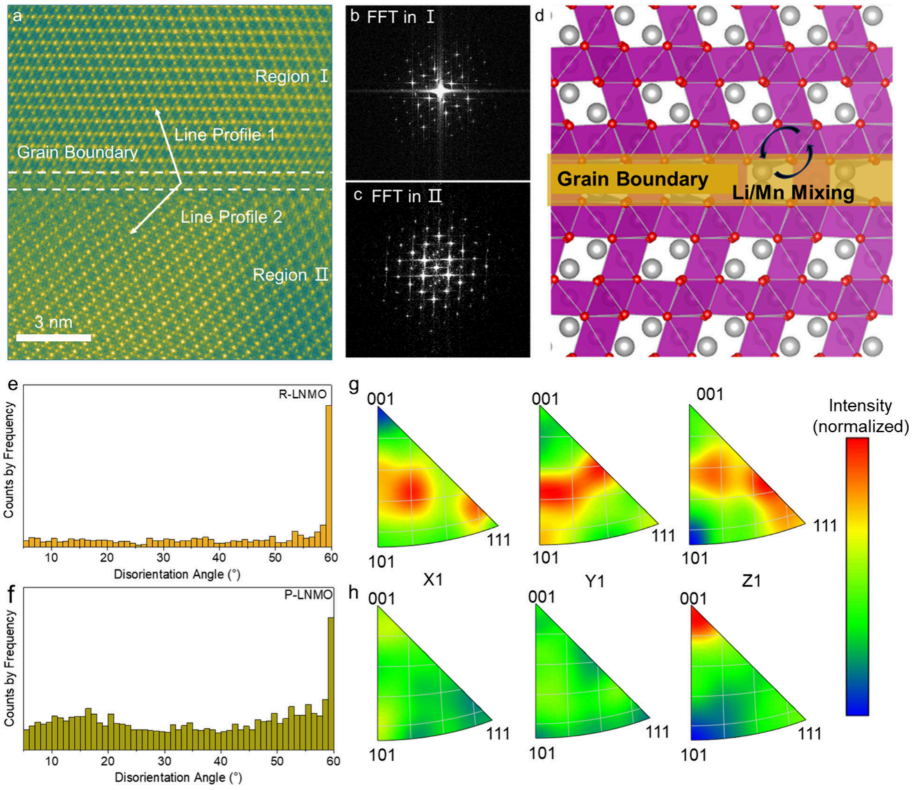

Figure 5. Evidence of twining defects and preferred grain orientations in regenerated cathodes. (a) HAADF-STEM images of the grain boundary in the R-LNMO particle. (b, c) Fast Fourier transform (FFT) images of regions in a. (d) Structure schematic of the twining grain boundary (Li, Mn, and O). (e, f) The disorientation angle distribution in R-LNMO and P-LNMO. (g, h) The inverse pole figures (IPF) in the *x*, *y*, and *z* directions in R-LNMO and P-LNMO. The color bar refers to the intensity of the IPF pole figure.

The DCIR was measured at different SOC values and normalized by the capacity of individual cells. These values represent the average from repeated tests in three cells after different current pulses at 0.5C, 1C, and 2C (see details in the methods). The R_{DCIR} value comprises R_{i} (series resistance), R_{ct} (charge transfer resistance), and R_{diff} (diffusion resistance).[49] Given that the morphology and electrode−electrolyte interface of R-LNMO are identical to those of the pristine sample, the variation in determined R_{DCIR} can be considered to represent the difference in Li^+ diffusivity among samples. As depicted in Figure 4f, the highest DCIR value was detected in L-LNMO, owing to the impedance by its imperfect cation mixing. Intuitively, the lower R_{DCIR} across the entire SOC range indicates that R-LNMO has rapid lithium-ion diffusion kinetics compared with the pristine sample. Although such a variation in Li^+ diffusion resulting from defect engineering is valuable, understanding the structural properties required for this improvement is vital for future progress.

Li^+ Diffusion Dominated by Induced Defects. To gain a more precise understanding of the underlying structure and electrochemical behavior of regenerated LNMO particles at the atomic level, we conducted further characterization using spherical aberration-corrected STEM measurements. Upon revisiting the microstructure of R-LNMO (Figure 5a), a prominent feature emerged in the lattice-twinning structures accompanied by a substantial number of twin boundaries. The asymmetrical twinning structure in R-LNMO reveals that the upper and lower variants are connected via an operation of reflection and an additional shift along the {111} mirror plane.[17] Consequently, the {111} planes become staggered, crossing the twin boundary (highlighted by white lines). In Figure 5b−c, the FFT images of two regions demonstrate the different orientations of the bulk across the twinning feature. In Figure S20, two-line profiles extracted from the twinning structures demonstrate that the intensities of Mn atoms located at the twin boundaries are weaker than those in the bulk region (indicated by blue dashed lines as a guide). This observation implies that lithium will occupy the Mn sites at twinning boundaries rather than the surface region in the regenerated LNMO, resulting in the decreased intensity of these columns (Figure 5d). This insight underscores the accommodation of Li/Mn disordering and the presence of twin boundary defects in regenerated LNMO, which is considered as a key reason for enhanced intergranular Li^+ diffusion.

To further elucidate the structural merits of regenerated cathodes, we conducted an electron backscatter diffraction (EBSD) experiment to statistically analyze the crystallographic features. To quantify grain orientation and morphologies across the entire cross-section of the LNMO particles, the EBSD test was performed following a milling process by Plasma Focused Ion Beam (PFIB). The selected cleanup area for both samples is depicted in Figure S21. In the context of a cubic crystal, applying possible symmetries, the misorientation between two adjacent grains can be reduced to the disorientation angle ranging from 0°−62.80°.[50] Notably, Figure 5e illustrates a distinct peak present in the regenerated cathode at around 60°, corresponding to the twin $\sum 3/\langle 111 \rangle$ boundaries.[51] In comparison, the pristine LNMO exhibits more random grain disorientation at lower angles (Figure 5f). Li^+ diffuses from one tetrahedral site to an adjacent one through an octahedral vacancy surrounded by six Mn ions at the octahedral site, forming a channel perpendicular to the {111} surface.[17] The energy barrier for this channel is primarily influenced by the surrounding six Mn ions. Notably, the energy barrier for Li^+ diffusion along the twin boundary is lower than in the bulk region in spinel type structure.[17] This observation is consistent with the electrochemical behavior of R-LNMO-4, as the diminished twin boundaries after high-temperature annealing lead to altered diffusion properties. Thus, the induced twin boundaries contribute to the divergence in Li^+ diffusion in the regenerated LNMO samples.

Furthermore, it has been observed that the electrochemical properties, especially the rate performance, are also influenced by the preferred crystallographic planes in spinel-type cathodes.[52] As a primary outcome of the annealing step, the recrystallization enables the growth of preferential crystallographic planes in regenerated samples.[52] A significant increase in average grain size is noted in regenerated cathodes (0.45 μm) compared to the pristine sample (0.35 μm), indicating crystal regrowth following the annealing step (Figure S22). In the Inverse Pole Figures (IPF) mapping (Figure 5g,h), unlike the predominantly <001>-oriented grains observed in pristine samples, preferred <111>-oriented grains appear in regenerated cathodes. Additionally, from the X-ray diffraction pattern (XRD), an enhancement of the relative peak intensity between the (111) peak and the (311) peak in regenerated samples is observed (Figure S23). Preferred {111} facet facilitates the efficiency for intragranular Li^+ diffusion.[53,54] Therefore, the defect control step, combined with twin boundaries and preferred crystalline facets, results in a distinct rate performance, facilitating rapid Li^+ diffusion.

CONCLUSION

In summary, our study comprehensively investigated the mechanisms of rejuvenation for high-voltage spinel-type cathodes by the systematic control and tuning of composition and structural defects. Through advanced characterization methods, we illustrated the existence of Li/Mn disordering during the relithiation step, which contributes to the failure to restore electrochemical performance. In addition to mitigating Li/Mn disordering, the induction of twin boundaries and preferred grain regrowth, identified through STEM and EBSD techniques, effectively promotes intergranular lithium-ion diffusion in a defect engineering step via controlled short annealing. Significantly, the resulting regenerated LNMO demonstrates a substantial enhancement in its rate performance without sacrificing energy density at low rates, retaining 97.4% capacity after 100 cycles and 87.96% after 200 cycles at C/3. This effective direct recycling method, by leveraging defect control, not only provides a systematic understanding of the healing mechanism in spinel structures but also integrates defect engineering into the cathode design of primary synthesis, thereby enhancing the sustainability of next-generation LIBs.

EXPERIMENTAL SECTION

Materials. The pristine LNMO particle were obtained from Haldor Topsoe corporation, Denmark. The spent LNMO cathode were harvested from a multilayer LNMO/graphite pouch cell (>3Ah) cycled between 2.8 and 4.8 V at 0.33 C for more than 350 cycles. The standards for TEM-EELS, Mn_2O_3, and MnO_2 were purchased from Sigma-Aldrich.

Cathode Harvesting. All of the pouch cells were discharged to 2.8 V before disassembly. The cathode strips were harvested by thoroughly rinsing with dimethyl carbonate (DMC) and then soaked in NMP for 6 h under 50 °C. The active materials, binder, and carbon black were removed from the aluminum substrates by sonification and scrapping. Active materials were precipitated after centrifugation at 3500 rpm for 5 min. The precipitated active materials were then repeatedly washed several times with NMP by dispersion and centrifugation. Then the active materials were collected and dried under a vacuum at 80 °C overnight for regeneration.

Regeneration of Cathode Materials. The collected S-LNMO particles underwent lithiation via a hydrothermal treatment. Specifically, 0.25 g of S-LNMO was placed into a 100 mL Teflon-lined autoclave containing 80 mL of lithium hydroxide (LiOH) solution at various concentrations. The autoclaves were heated at 180 °C for 6 h. After naturally cooling to room temperature, the treated powders were washed at least five times with deionized water until the pH was approximately 7, and then dried under a vacuum at 80 °C overnight. The samples treated in 0.1 M, 1 M, and 4 M LiOH solutions are referred to as "L-LNMO-1", "L-LNMO-2", and "L-LNMO-3", respectively.

Based on ICP measurements, L-LNMO-2, with the correct stoichiometry, was selected for further treatment. L-LNMO was then annealed at different temperatures for 4 h, with a ramping rate of 5 °C/min under a 1 L/min oxygen flow. The annealed samples at 650 °C, 750 °C, 850 °C, and 950 °C are labeled as "R-LNMO-1", "R-LNMO-2", "R-LNMO-3", and "R-LNMO-4", respectively. Among these, R-LNMO-3 exhibited the best electrochemical performance under optimal regeneration conditions.

Materials Characterization. The chemical composition of LNMO powders was evaluated by inductively coupled plasma mass spectrometry (ICP–MS, Thermo Scientific, iCAP RQ model). Their crystal structures were examined by X-ray powder diffraction (XRD) employing a Bruker D2 Phaser (Cu Kα radiation, λ = 1.5406 Å). The morphology of the LNMO powders was observed by an FEI Apreo LoVac scanning electron microscope (SEM) with an X-Max 80 EDS detector.

Time-of-flight (TOF) powder neutron diffraction was measured with the VULCAN instrument at the Spallation Neutron Sources (SNS), Oak Ridge National Laboratory (ORNL). The diffraction pattern was measured at the detector banks at $2\theta = \pm 90°$, equipped with 5 mm receiving collimators. Neutron powder diffraction patterns were collected in the high-intensity mode ($\Delta d/d \approx 0.45\%$) for a duration of 2 h under nominal 1.4 MW SNS operation and then processed using VDRIVE software. Rietveld refinement against the neutron diffraction was performed by using General Structure Analysis System (GSAS) software with the EXPGUI interface.

X-ray photoelectron spectroscopic (XPS) measurement was conducted with an AXIS Supra by Kratos Analytical instrument with an Al Ka anode source working at 15 kV and 10−8 Torr chamber pressure. The spectra data were processed with CasaXPS software. All spectra were calibrated with the hydrocarbon C 1s peak at 284.6 eV. Aberration corrected scanning transmission electron microscopy (AC-STEM) was conducted by using a JEOL JEM-ARM 300F at 300 kV.

TEM-EELS characterizations were performed using a ThermoFisher Talos 200X TEM electron microscope system operating at an accelerating voltage of 200 kV. The system was equipped with a Schottky X-ray FEG field emission electron gun, a Gatan Continuum (1069) EELS spectrometer, a STEM model, 4 in-column SDD Super-X detectors, and a Ceta camera. Additionally, the TALOS microscope was outfitted with a high-resolution Gatan imaging filter (Gatan Continuum 1069) for EELS mapping with a probe current of approximately 140 pA for EELS maps.

Soft X-ray absorption spectroscopy (soft XAS) was performed at Beamline 8-2 of the Stanford Synchrotron Radiation Lightsource (SSRL). Data acquisition occurred under ultrahigh-vacuum conditions (10^{-9} Torr) at room temperature, with an energy resolution of approximately 0.2 eV and a beam spot size of about 1 mm^2. Samples were mounted on an aluminum sample holder inside an argon-filled glovebox and securely sealed during transfer. The soft XAS data were analyzed using Pymca, normalized to a range of [0,1].

Spectroscopic transmission X-ray microscopy (TXM) was performed at the 6-2c beamline at the Stanford Synchrotron Radiation Light source (SSRL). 8.95 keV X-rays (8.95 keV) were utilized to characterize the particle morphology. The LNMO particles were placed in a quartz tube and sealed with epoxy in an Ar-filled glovebox. The tomography data were taken over an angular range of 180°. The field of view of each tile was 16 μm, consisting of 1024 × 1024 pixels with a pixel size of 28.7 nm. The images were then processed in the TXM-Wizard software suite, with reference correction, energy average, image alignment, and 2D X-ray absorption near-edge structure (2D XANES) analysis. The edge energy maps saved by TXM-Wizard were exported into 64-bit.raw files by using MATLAB for visualization.

The cross-section microstructures of LNMO particles were characterized by a Helios G4 PFIB UXe DualBeam plasma focused ion beam/scanning electron microscope (P-FIB/SEM) with a xenon source and electron backscatter diffraction (EBSD) detector. Sample milling was conducted at 30 kV with a 2.5 μA current. Afterward, a lower current (500 and 60 nA) was used to polish the cross-section. Electron imaging was conducted at 5 kV and 4 nA beam conditions.

Electrochemical Testing. The electrochemical performance was evaluated by fabricating CR2032 half coin-cells assembled in an Ar-filled glovebox kept at <0.1 ppm of O_2 and <0.1 ppm of H_2O. The cathode electrode was prepared by casting the slurry composed of cathode powder, conductive agent (Super P65), and polyvinylidene fluoride (PVDF) with a mass ratio of 8:1:1 in *N*-methyl-2-pyrrolidone (NMP) solvent on an Al foil. After being dried at 120 °C for 12 h in a vacuum oven, it was punched and calendared. Coin cells were then made inside that glovebox with the prepared cathode (mass loading of ∼4.5 mg), Li metal as the anode, and LP57 (1.2 M LiPF6 in EC/EMC = 3:7) as the electrolyte. Galvanostatic charge−discharge was carried out using a Neware battery testing system in the potential range of 3.0−4.85 V at different rates for certain cycles after C/10 in the first 3 activation cycles. EIS tests of LNMO/Li coin cell with different SOCs were performed on a Biologic VSP-300 potentiostat with a 10 mV perturbation in the frequency range of 1 MHz to 100 mHz. The fitting of the EIS data was conducted via Z-view software. DRT was analyzed via MATLAB based DRT calculation code developed by T. H. Wan et al.[55] The direct current internal resistance (DCIR) experiment was performed by charging and discharging the cell at a constant current (0.1 C-rate) to different state-of-charge (SOC) (20%, 40%, 60%, and 80%) after 2 formation cycles. Thereafter, the process of applying a pulse current charge for 30 s, a rest for 10 min, a pulse current discharge for 30 s, and a rest for 10 min was repeated. The pulse current was applied in the following order: 0.5 C-, 1 C-, and 2 C-rate. Three cells were tested in parallel to account for variability and to generate error bars. All the C-rates for the electrochemical tests were based on the practical capacity of 135 mAh/g.

ASSOCIATED CONTENT

Supporting Information

The Supporting Information is available free of charge at https://pubs.acs.org/doi/10.1021/acsnano.4c10164.

> Additional materials characterizations, electrochemical performances, EIS analysis and Rietveld refinement results of neutron diffraction (PDF)

AUTHOR INFORMATION

Corresponding Author

Zheng Chen − *Program of Materials Science and Engineering, University of California San Diego, La Jolla, California 92093, United States; Aiiso Yufeng Li Family Department of Chemical and Nano Engineering and Sustainable Power & Energy Center (SPEC), University of California San Diego, La Jolla, California 92093, United States;* orcid.org/0000-0002-9186-4298; Email: zhc199@ucsd.edu

Authors

Hongpeng Gao − *Program of Materials Science and Engineering, University of California San Diego, La Jolla, California 92093, United States; Aiiso Yufeng Li Family Department of Chemical and Nano Engineering, University of California San Diego, La Jolla, California 92093, United States;* orcid.org/0000-0002-6640-4070

Bing Han − *Aiiso Yufeng Li Family Department of Chemical and Nano Engineering, University of California San Diego, La Jolla, California 92093, United States*

Duc Tran − *Aiiso Yufeng Li Family Department of Chemical and Nano Engineering, University of California San Diego, La Jolla, California 92093, United States;* orcid.org/0000-0003-0320-9929

Luqi Zhang − *Aiiso Yufeng Li Family Department of Chemical and Nano Engineering, University of California San Diego, La Jolla, California 92093, United States*

Zishuo Zhao − *School for Engineering of Matter, Transport, and Energy, Arizona State University, Tempe, Arizona 85287, United States*

Yu-ting Chen − *Program of Materials Science and Engineering, University of California San Diego, La Jolla, California 92093, United States; Aiiso Yufeng Li Family Department of Chemical and Nano Engineering, University of California San Diego, La Jolla, California 92093, United States*

Wei Tang − *Aiiso Yufeng Li Family Department of Chemical and Nano Engineering, University of California San Diego, La Jolla, California 92093, United States*

Mingjie Xu − *Irvine Material Research Institute, University of California Irvine, Irvine, California 92697, United States*

Junlin Wu − *Program of Materials Science and Engineering, University of California San Diego, La Jolla, California 92093, United States; Aiiso Yufeng Li Family Department of Chemical and Nano Engineering, University of California San Diego, La Jolla, California 92093, United States*

Xiaolu Yu − *Program of Materials Science and Engineering, University of California San Diego, La Jolla, California 92093, United States; Aiiso Yufeng Li Family Department of Chemical and Nano Engineering, University of California San Diego, La Jolla, California 92093, United States*

Varun Gupta − *Program of Materials Science and Engineering, University of California San Diego, La Jolla, California 92093, United States; Aiiso Yufeng Li Family Department of Chemical and Nano Engineering, University of California San Diego, La Jolla, California 92093, United States;* orcid.org/0000-0002-4976-8593

Maura Appleberry − *Aiiso Yufeng Li Family Department of Chemical and Nano Engineering, University of California San Diego, La Jolla, California 92093, United States*

Haodong Liu − *Aiiso Yufeng Li Family Department of Chemical and Nano Engineering, University of California San Diego, La Jolla, California 92093, United States*

Yijie Yin − *Program of Materials Science and Engineering, University of California San Diego, La Jolla, California 92093, United States; Aiiso Yufeng Li Family Department of Chemical and Nano Engineering, University of California San Diego, La Jolla, California 92093, United States*

Weiliang Yao − *Aiiso Yufeng Li Family Department of Chemical and Nano Engineering, University of California San Diego, La Jolla, California 92093, United States*

Mingqian Li − *Aiiso Yufeng Li Family Department of Chemical and Nano Engineering, University of California*

San Diego, La Jolla, California 92093, United States; orcid.org/0000-0001-6726-5757

Weikang Li − *Aiiso Yufeng Li Family Department of Chemical and Nano Engineering, University of California San Diego, La Jolla, California 92093, United States*

Linqin Mu − *School for Engineering of Matter, Transport, and Energy, Arizona State University, Tempe, Arizona 85287, United States;* orcid.org/0000-0003-4421-4820

Ying Shirley Meng − *Program of Materials Science and Engineering, University of California San Diego, La Jolla, California 92093, United States; Aiiso Yufeng Li Family Department of Chemical and Nano Engineering and Sustainable Power & Energy Center (SPEC), University of California San Diego, La Jolla, California 92093, United States;* orcid.org/0000-0001-8936-8845

Complete contact information is available at:
https://pubs.acs.org/10.1021/acsnano.4c10164

Notes

The authors declare no competing financial interest.

ACKNOWLEDGMENTS

This work was supported by the start-up fund support from the Jacob School of Engineering at UC San Diego. Neutron diffraction work was carried out at the Spallation Neutron Source (SNS), which is the U.S. DOE user facility at the Oak Ridge National Laboratory, sponsored by the Scientific User Facilities Division, Office of Basic Energy Sciences (BES). The authors acknowledge Dr. Yan Chen and Dr. Dunji Yu for the help with data acquisition. Use of the Stanford Synchrotron Radiation Light source, SLAC National Accelerator Laboratory, is supported by the U.S. Department of Energy, Office of Science, Office of Basic Energy Sciences, under Proposal No. S-XV-ST-5823. The authors acknowledge the use of a shared TEM facility at the UC Irvine Materials Research Institute (IMRI), which is supported in part by the National Science Foundation through the UC Irvine Materials Research Science and Engineering Center (UCI MRSEC DMR-2011967), as well as the Nano3/SDNI and IMCF facilities and instrumentation supported by the National Science Foundation (ECCS-1542148 and UCSD MRSEC DMR-2011924) at UC San Diego for specimen preparation. The authors acknowledge Dr. Amir Avishai and Dr. Johanna L. Nelson Weker for the help with data acquisition and analysis.

REFERENCES

(1) Chu, S.; Cui, Y.; Liu, N. The path towards sustainable energy. *Nat. Mater.* **2017**, *16* (1), 16−22.

(2) Tran, M. K.; Rodrigues, M.-T. F.; Kato, K.; Babu, G.; Ajayan, P. M. Deep eutectic solvents for cathode recycling of Li-ion batteries. *Nature Energy* **2019**, *4* (4), 339−345.

(3) Schmuch, R.; Wagner, R.; Hörpel, G.; Placke, T.; Winter, M. Performance and cost of materials for lithium-based rechargeable automotive batteries. *Nature Energy* **2018**, *3* (4), 267−278.

(4) Duffner, F.; Kronemeyer, N.; Tübke, J.; Leker, J.; Winter, M.; Schmuch, R. Post-lithium-ion battery cell production and its compatibility with lithium-ion cell production infrastructure. *Nature Energy* **2021**, *6* (2), 123−134.

(5) Li, W.; Cho, Y.-G.; Yao, W.; Li, Y.; Cronk, A.; Shimizu, R.; Schroeder, M. A.; Fu, Y.; Zou, F.; Battaglia, V.; Manthiram, A.; Zhang, M.; Meng, Y. S. Enabling high areal capacity for Co-free high voltage spinel materials in next-generation Li-ion batteries. *J. Power Sources* **2020**, 473, 228579.

(6) Li, W.; Cheng, D.; Shimizu, R.; Li, Y.; Yao, W.; Raghavendran, G.; Zhang, M.; Meng, Y. S. Artificial cathode electrolyte interphase for improving high voltage cycling stability of thick electrode with Co-free 5 V spinel oxides. *Energy Storage Materials* **2022**, *49*, 77−84.

(7) Yu, X. Releasing oxygen from the bulk. *Nature Energy* **2021**, *6* (6), 572−573.

(8) Park, S. H.; Oh, S. W.; Kang, S. H.; Belharouak, I.; Amine, K.; Sun, Y. K. Comparative study of different crystallographic structure of LiNi$_{0.5}$Mn$_{1.5}$O$_{4-\delta}$ cathodes with wide operation voltage (2.0−5.0V). *Electrochim. Acta* **2007**, *52* (25), 7226−7230.

(9) Spence, S. L.; Xu, Z.; Sainio, S.; Nordlund, D.; Lin, F. Tuning the Morphology and Electronic Properties of Single-Crystal LiNi$_{0.5}$Mn$_{1.5}$O$_{4-\delta}$: Exploring the Influence of LiCl-KCl Molten Salt Flux Composition and Synthesis Temperature. *Inorg. Chem.* **2020**, *59* (15), 10591−10603.

(10) Yao, W.; Chouchane, M.; Li, W.; Bai, S.; Liu, Z.; Li, L.; Chen, A. X.; Sayahpour, B.; Shimizu, R.; Raghavendran, G.; et al. A 5 V-class cobalt-free battery cathode with high loading enabled by dry coating. *Energy Environ. Sci.* **2023**, *16* (4), 1620−1630.

(11) Jang, J.; Chen, Y.-T.; Deysher, G.; Cheng, D.; Ham, S.-Y.; Cronk, A.; Ridley, P.; Yang, H.; Sayahpour, B.; Han, B.; Li, W.; Yao, W.; Wu, E. A.; Doux, J.-M.; Nguyen, L. H. B.; Oh, J. A. S.; Tan, D. H. S.; Meng, Y. S. Enabling a Co-Free, High-Voltage LiNi$_{0.5}$Mn$_{1.5}$O$_4$ Cathode in All-Solid-State Batteries with a Halide Electrolyte. *ACS Energy Letters* **2022**, *7* (8), 2531−2539.

(12) Fehse, M.; Etxebarria, N.; Otaegui, L.; Cabello, M.; Martín-Fuentes, S.; Cabañero, M. A.; Monterrubio, I.; Elkjær, C. F.; Fabelo, O.; Enkubari, N. A.; López del Amo, J. M.; Casas-Cabanas, M.; Reynaud, M. Influence of Transition-Metal Order on the Reaction Mechanism of LNMO Cathode Spinel: An Operando X-ray Absorption Spectroscopy Study. *Chem. Mater.* **2022**, *34* (14), 6529−6540.

(13) He, J.; Melinte, G.; Darma, M. S. D.; Hua, W.; Das, C.; Schokel, A.; Etter, M.; Hansen, A.-L.; Mereacre, L.; Geckle, U.; Bergfeldt, T.; Sun, Z.; Knapp, M.; Ehrenberg, H.; Maibach, J. Surface Structure Evolution and its Impact on the Electrochemical Performances of Aqueous-Processed High-Voltage Spinel LiNi$_{0.\ 5}$Mn$_{1.\ 5}$O$_4$ Cathodes in Lithium-Ion Batteries. *Adv. Funct. Mater.* **2022**, *32* (46), 2207937.

(14) Xiao, J.; Chen, X.; Sushko, P. V.; Sushko, M. L.; Kovarik, L.; Feng, J.; Deng, Z.; Zheng, J.; Graff, G. L.; Nie, Z.; Choi, D.; Liu, J.; Zhang, J.; Whittingham, M. S. High-Performance LiNi$_{0.5}$Mn$_{1.5}$O$_4$ Spinel Controlled by Mn^{3+} Concentration and Site Disorder. *Adv. Mater.* **2012**, *24* (16), 2109−2116.

(15) Kim, J. W.; Kim, D. H.; Oh, D. Y.; Lee, H.; Kim, J. H.; Lee, J. H.; Jung, Y. S. Surface chemistry of LiNi$_{0.5}$Mn$_{1.5}$O$_4$ particles coated by Al$_2$O3 using atomic layer deposition for lithium-ion batteries. *J. Power Sources* **2015**, *274*, 1254−1262.

(16) Piao, N.; Wang, P.-F.; Chen, L.; Deng, T.; Fan, X.; Wang, L.; He, X. Nonflammable all-fluorinated electrolytes enabling high-power and long-life LiNi$_{0.5}$Mn$_{1.5}$O$_4$/Li$_4$Ti$_5$O$_{12}$ lithium-ion batteries. *Nano Energy* **2023**, *105*, 108040.

(17) Wang, R.; Chen, X.; Huang, Z.; Yang, J.; Liu, F.; Chu, M.; Liu, T.; Wang, C.; Zhu, W.; Li, S.; Li, S.; Zheng, J.; Chen, J.; He, L.; Jin, L.; Pan, F.; Xiao, Y. Twin boundary defect engineering improves lithium-ion diffusion for fast-charging spinel cathode materials. *Nat. Commun.* **2021**, *12* (1), 3085.

(18) Gao, H.; Yan, Q.; Tran, D.; Yu, X.; Liu, H.; Li, M.; Li, W.; Wu, J.; Tang, W.; Gupta, V.; Luo, J.; Chen, Z. Upcycling of Spent LiNi$_{0.33}$Co$_{0.33}$Mn$_{0.33}$O$_2$ to Single-Crystal Ni-Rich Cathodes Using Lean Precursors. *ACS Energy Letters* **2023**, *8* (10), 4136−4144.

(19) Yu, X.; Yu, S.; Yang, Z.; Gao, H.; Xu, P.; Cai, G.; Rose, S.; Brooks, C.; Liu, P.; Chen, Z. Achieving low-temperature hydrothermal relithiation by redox mediation for direct recycling of spent lithium-ion battery cathodes. *Energy Storage Materials* **2022**, *51*, 54−62.

(20) Xu, P.; Yang, Z.; Yu, X.; Holoubek, J.; Gao, H.; Li, M.; Cai, G.; Bloom, I.; Liu, H.; Chen, Y.; An, K.; Pupek, K.; Liu, P.; Chen, Z. Design and Optimization of the Direct Recycling of Spent Li-Ion

Battery Cathode Materials. *ACS Sustainable Chem. Eng.* **2021**, *9* (12), 4543−4553.

(21) Hawley, W. B.; Parejiya, A.; Bai, Y.; Meyer, H. M.; Wood, D. L.; Li, J. Lithium and transition metal dissolution due to aqueous processing in lithium-ion battery cathode active materials. *J. Power Sources* **2020**, *466*, 228315.

(22) Gao, H.; Yan, Q.; Xu, P.; Liu, H.; Li, M.; Liu, P.; Luo, J.; Chen, Z. Efficient Direct Recycling of Degraded $LiMn_2O_4$ Cathodes by One-Step Hydrothermal Relithiation. *ACS Appl. Mater. Interfaces* **2020**, *12* (46), 51546−51554.

(23) Qin, Z.; Zhang, Y.; Luo, W.; Zhang, T.; Wang, T.; Ni, L.; Wang, H.; Zhang, N.; Liu, X.; Zhou, J.; Chen, G. A Universal Molten Salt Method for Direct Upcycling of Spent Ni-rich Cathode towards Single-crystalline Li-rich Cathode. *Angew. Chem., Int. Ed.* **2023**, *62* (25), No. e202218672.

(24) Meng, X.; Hao, J.; Cao, H.; Lin, X.; Ning, P.; Zheng, X.; Chang, J.; Zhang, X.; Wang, B.; Sun, Z. Recycling of $LiNi_{1/3}Co_{1/3}Mn_{1/3}O_2$ cathode materials from spent lithium-ion batteries using mechanochemical activation and solid-state sintering. *Waste Management* **2019**, *84*, 54−63.

(25) Wang, M.; Tan, Q.; Liu, L.; Li, J. Efficient separation of aluminum foil and cathode materials from spent lithium-ion batteries using a low-temperature molten salt. *ACS sustainable chemistry & engineering* **2019**, *7* (9), 8287−8294.

(26) Wang, T.; Luo, H.; Bai, Y.; Li, J.; Belharouak, I.; Dai, S. Direct Recycling of Spent NCM Cathodes through Ionothermal Lithiation. *Adv. Energy Mater.* **2020**, *10* (30), 2001204.

(27) Park, K.; Yu, J.; Coyle, J.; Dai, Q.; Frisco, S.; Zhou, M.; Burrell, A. Direct Cathode Recycling of End-Of-Life Li-Ion Batteries Enabled by Redox Mediation. *ACS Sustainable Chem. Eng.* **2021**, *9* (24), 8214−21.

(28) Xu, P.; Dai, Q.; Gao, H.; Liu, H.; Zhang, M.; Li, M.; Chen, Y.; An, K.; Meng, Y. S.; Liu, P.; Li, Y.; Spangenberger, S. J.; Gaines, L.; Lu, J.; Chen, Z. Efficient Direct Recycling of Lithium-Ion Battery Cathodes by Targeted Healing. *Joule* **2020**, *4* (12), 2609−2626.

(29) Shi, Y.; Chen, G.; Chen, Z. Effective regeneration of $LiCoO_2$ from spent lithium-ion batteries: a direct approach towards high-performance active particles. *Green Chem.* **2018**, *20* (4), 851−862.

(30) Lin, J.; Fan, E.; Zhang, X.; Li, Z.; Dai, Y.; Chen, R.; Wu, F.; Li, L. Sustainable Upcycling of Spent Lithium-Ion Batteries Cathode Materials: Stabilization by In Situ Li/Mn Disorder. *Adv. Energy Mater.* **2022**, *12* (26), 2201174.

(31) Wang, D.; Gao, C.; Zhou, X.; Peng, S.; Tang, M.; Wang, Y.; Huang, L.; Yang, W.; Gao, X. Enhancing reversibility of $LiNi_{0.5}Mn_{1.5}O_4$ by regulating surface oxygen deficiency. *Carbon Energy* **2023**, *5*, No. e338.

(32) Ding, H.; Wang, P.; Zhang, N.; Zhou, J.; Li, X.; Li, C.; Zhao, D.; Li, S. Improving electrochemical performances of $LiNi_{0.5}Mn_{1.5}O_4$ by the strategy of oxygen vacancy doping. *Applied Materials Today* **2024**, *38*, 102248.

(33) Jiang, H.; Zeng, C.; Zhu, W.; Luo, J.; Liu, Z.; Zhang, J.; Liu, R.; Xu, Y.; Chen, Y.; Hu, W. Boosting cycling stability by regulating surface oxygen vacancies of LNMO by rapid calcination. *Nano Research* **2024**, *17* (4), 2671−2677.

(34) Sun, H.; Hu, A.; Spence, S.; Kuai, C.; Hou, D.; Mu, L.; Liu, J.; Li, L.; Sun, C.; Sainio, S.; Nordlund, D.; Luo, W.; Huang, Y.; Lin, F. Tailoring disordered/ordered phases to revisit the degradation mechanism of high-voltage $LiNi_{0.5}Mn_{1.5}O_4$ spinel cathode materials. *Adv. Funct. Mater.* **2022**, *32* (21), 2112279.

(35) Gao, C.; Liu, H.; Zhang, J.; Guo, Z.; Huang, H. Simplified crystal grain boundary engineering of solid electrolyte-infused $LiNi_{0.5}Mn_{1.5}O_4$ cathodes for high cycling stability lithium-ion batteries. *J. Power Sources* **2023**, *582*, 233434.

(36) Stüble, P.; Mereacre, V.; Geßwein, H.; Binder, J. R. On the Composition of $LiNi_{0.5}Mn_{1.5}O_4$ Cathode Active Materials. *Adv. Energy Mater.* **2023**, *13* (10), 2203778.

(37) Zhu, X.; Schülli, T. U.; Yang, X.; Lin, T.; Hu, Y.; Cheng, N.; Fujii, H.; Ozawa, K.; Cowie, B.; Gu, Q.; Zhou, S.; Cheng, Z.; Du, Y.; Wang, L. Epitaxial growth of an atom-thin layer on a $LiNi_{0.5}Mn_{1.5}O_4$ cathode for stable Li-ion battery cycling. *Nat. Commun.* **2022**, *13* (1), 1565.

(38) Gupta, V.; Yu, X.; Gao, H.; Brooks, C.; Li, W.; Chen, Z. Scalable Direct Recycling of Cathode Black Mass from Spent Lithium-Ion Batteries. *Adv. Energy Mater.* **2023**, *13* (6), 2203093.

(39) Kim, J.-H.; Myung, S.-T.; Yoon, C.; Kang, S.; Sun, Y.-K. Comparative study of $LiNi_{0.5}Mn_{1.5}O_{4-\delta}$ and $LiNi_{0.5}Mn_{1.5}O_4$ cathodes having two crystallographic structures: fd $\bar{3}$ m and P 4332. *Chemistry of materials* **2004**, *16* (5), 906−914.

(40) Choi, H. W.; Kim, S. J.; Rim, Y.-H.; Yang, Y. S. Effect of Lithium Deficiency on Lithium-Ion Battery Cathode $Li_xNi_{0.5}Mn_{1.5}O_4$. *J. Phys. Chem. C* **2015**, *119* (49), 27192−27199.

(41) Pang, W. K.; Lu, C.-Z.; Liu, C.-E.; Peterson, V. K.; Lin, H.-F.; Liao, S.-C.; Chen, J.-M. Crystallographic origin of cycle decay of the high-voltage $LiNi_{0.5}Mn_{1.5}O_4$ spinel lithium-ion battery electrode. *Phys. Chem. Chem. Phys.* **2016**, *18* (26), 17183−17189.

(42) Sushko, P. V.; Rosso, K. M.; Zhang, J. G.; Liu, J.; Sushko, M. L. Oxygen Vacancies and Ordering of d-levels Control Voltage Suppression in Oxide Cathodes: the Case of Spinel $LiNi_{0.5}Mn_{1.5}O_{4-\delta}$. *Adv. Funct. Mater.* **2013**, *23* (44), 5530−5535.

(43) Lee, Y.; Shin, J.; Kang, H.; Lee, D.; Kim, T. H.; Kwon, Y. K.; Cho, E. Promoting the Reversible Oxygen Redox Reaction of Li-Excess Layered Cathode Materials with Surface Vanadium Cation Doping. *Advanced Science* **2021**, *8* (6), 2003013.

(44) Jo, M. R.; Kim, Y. I.; Kim, Y.; Chae, J. S.; Roh, K. C.; Yoon, W. S.; Kang, Y. M. Lithium-Ion Transport through a Tailored Disordered Phase on the $LiNi_{0.5}Mn_{1.5}O_4$ Surface for High-Power Cathode Materials. *ChemSusChem* **2014**, *7* (8), 2248−2254.

(45) Sun, H.; Hu, A.; Spence, S.; Kuai, C.; Hou, D.; Mu, L.; Liu, J.; Li, L.; Sun, C.; Sainio, S.; Nordlund, D.; Luo, W.; Huang, Y.; Lin, F. Tailoring Disordered/Ordered Phases to Revisit the Degradation Mechanism of High-Voltage $LiNi_{0.5}Mn_{1.5}O_4$ Spinel Cathode Materials. *Adv. Funct. Mater.* **2022**, *32* (21), 2112279.

(46) Gao, X.; Ikuhara, Y. H.; Fisher, C. A.; Moriwake, H.; Kuwabara, A.; Oki, H.; Kohama, K.; Yoshida, R.; Huang, R.; Ikuhara, Y. Structural distortion and compositional gradients adjacent to epitaxial $LiMn_2O_4$ thin film interfaces. *Advanced Materials Interfaces* **2014**, *1* (8), 1400143.

(47) Shin, D. W.; Bridges, C. A.; Huq, A.; Paranthaman, M. P.; Manthiram, A. Role of Cation Ordering and Surface Segregation in High-Voltage Spinel $LiMn_{1.5}Ni_{0.5-x}M_xO_4$ (M= Cr, Fe, and Ga) Cathodes for Lithium-Ion Batteries. *Chem. Mater.* **2012**, *24* (19), 3720−3731.

(48) Aktekin, B.; Massel, F.; Ahmadi, M.; Valvo, M.; Hahlin, M.; Zipprich, W.; Marzano, F.; Duda, L.; Younesi, R.; Edström, K.; Brandell, D. How Mn/Ni Ordering Controls Electrochemical Performance in High-Voltage Spinel $LiNi_{0.44}Mn_{1.56}O_4$ with Fixed Oxygen Content. *ACS Applied Energy Materials* **2020**, 3 (6), 6001−6013.

(49) Lee, W.; Lee, S.; Lee, E.; Choi, M.; Thangavel, R.; Lee, Y.; Yoon, W.-S. Destabilization of the surface structure of Ni-rich layered materials by water-washing process. *Energy Storage Materials* **2022**, *44*, 441−451.

(50) Priester, L. *Grain Boundaries: From Theory to Engineering*; Springer: New York, 2013.

(51) Parajuli, P.; Mendoza-Cruz, R.; Santiago, U.; Ponce, A.; Yacamán, M. J. The evolution of growth, crystal orientation, and grain boundaries disorientation distribution in gold thin films. *Crystal Research and Technology* **2018**, *53* (8), 1800038.

(52) Quinn, A.; Moutinho, H.; Usseglio-Viretta, F.; Verma, A.; Smith, K.; Keyser, M.; Finegan, D. P. Electron Backscatter Diffraction for Investigating Lithium-Ion Electrode Particle Architectures. *Cell Reports Physical Science* **2020**, *1* (8), 100137.

(53) Jiang, C.; Tang, Z.; Wang, S.; Zhang, Z. A truncated octahedral spinel $LiMn_2O_4$ as high-performance cathode material for ultrafast and long-life lithium-ion batteries. *J. Power Sources* **2017**, *357*, 144−148.

(54) Xu, C.; Li, J.; Feng, X.; Zhao, J.; Tang, C.; Ji, B.; Hu, J.; Cao, C.; Zhu, Y.; Butt, F. K. The improved performance of spinel $LiMn_2O_4$

cathode with micro-nanostructured sphere-interconnected-tube morphology and surface orientation at extreme conditions for lithium-ion batteries. *Electrochim. Acta* **2020**, *358*, 136901.

(55) Wan, T. H.; Saccoccio, M.; Chen, C.; Ciucci, F. Influence of the Discretization Methods on the Distribution of Relaxation Times Deconvolution: Implementing Radial Basis Functions with DRTtools. *Electrochim. Acta* **2015**, *184*, 483−499.